Modeling laser-driven electron acceleration using WARP with Fourier decomposition

P. Lee[a], T. L. Audet[a], R. Lehe[b], J.-L.Vay[b], G. Maynard[a], B. Cros[a]

[a] *LPGP, CNRS, Univ. Paris-Sud, Université Paris-Saclay, 91405, Orsay, France*
[b] *Lawrence Berkeley National Laboratory, Berkeley, CA 94720, USA*

Abstract

WARP is used with the recent implementation of the Fourier decomposition algorithm to model laser-driven electron acceleration in plasmas. Simulations were carried out to analyze the experimental results obtained on ionization-induced injection in a gas cell. The simulated results are in good agreement with the experimental ones, confirming the ability of the code to take into account the physics of electron injection and reduce calculation time. We present a detailed analysis of the laser propagation, the plasma wave generation and the electron beam dynamics.

Keywords: LPA, PIC, WARP, Ionization-induced injection

1. Introduction

A kinetic description of the plasma is required in modeling laser-driven plasma electron acceleration (LPA) in the regimes currently explored in the experiments. In addition, the strongly nonlinear nature of these regimes are intrinsically three-dimensional, therefore a realistic description of the process requires the use of a three dimensional, kinetic approach. The Particle-in-Cell (PIC) technique which solves the Maxwell-Vlasov equations provides detailed information about the laser-plasma interaction. This technique constitutes the most powerful method to study this problem, however 3D simulations with PIC code demands extreme computer resources, pushing existing computers to their limits.

The recent development in PIC framework Warp [1] with the Fourier decomposition algorithm [2] has allowed a quasi 3D description of the LPA with a computational load that is similar to bi-dimensional calculations. We benefited from these advantages to analyze results from an experiment performed at the Lund Laser Center [3] on electron ionization-induced injection.

This article is organized as follows: we introduce briefly the theory of the Fourier decomposition algorithm [2, 4] in PIC code in Section 2; in Section 3, the simulation results are presented and a detailed analysis on the laser, the plasma waves and the beam dynamics from the simulations is presented.

2. Mathematical description of the Fourier decomposition algorithm in PIC code

We begin by decomposing the electromagnetic fields, the charge (ρ) and current densities $\mathbf{J}$, expressed in cylindrical coordinates (r, z, θ), into a Fourier series in θ,

$$\begin{aligned}\mathbf{F}(r,z,\theta) &= \Re\left(\sum_{m=0}\mathbf{F}^m(r,z)e^{im\theta}\right)\\ &= \mathbf{F}^0(r,z) + \Re\left(\mathbf{F}^1\right)\cos(\theta) - \Im\left(\mathbf{F}^1\right)\sin(\theta)\\ &\quad + \Re\left(\mathbf{F}^2\right)\cos(2\theta) - \Im\left(\mathbf{F}^2\right)\sin(2\theta)\\ &\quad + \dots\end{aligned} \tag{2.1}$$

The amplitudes of each Fourier harmonic (for all fields) $\mathbf{F}^m$ are complex, whereas the physical fields they are describing, $\mathbf{F}$, are real. The major advantage of this expansion is that it allows modeling of a linearly polarized laser with only the first harmonic [2, 4].

For a linearly polarized field, the axisymmetric laser fields, with amplitude $a(r, z, t)$ and propagating along z is expressed as::

$$\begin{aligned}\mathbf{E}(r,z,\theta,t) &= E_y(r,z,t)\widehat{y} = E_y[\cos(\theta)\widehat{e_r} - \sin(\theta)\widehat{e_\theta}],\\ \mathbf{B}(r,z,\theta,t) &= B_z(r,z,t)\widehat{x} = B_z[\cos(\theta)\widehat{e_r} + \sin(\theta)\widehat{e_\theta}].\end{aligned} \tag{2.2}$$

By equating the fields in Eq. 2.2 to the expansion in Eq. 2.1, one gets:

$$\begin{aligned}\mathrm{E}_r^1(r,z,t) &= a(r,z,t),\\ \mathrm{E}_\theta^1(r,z,t) &= -ia(r,z,t),\\ \mathrm{B}_r^1(r,z,t) &= ia(r,z,t),\\ \mathrm{B}_\theta^1(r,z,t) &= a(r,z,t).\end{aligned} \tag{2.3}$$

where only the mode, $m = 1$ contributes. This can be generalized to circularly or elliptically polarized lasers, by combining two linearly polarized lasers.

*patrick.lee@u-psud.fr

From Faraday's and Ampere's equations, the time-evolution of electromagnetic fields, written in normalized units, is given by:

$$\begin{aligned} \frac{\partial \mathbf{B}}{\partial t} &= -\nabla \times \mathbf{E}, \\ \frac{\partial \mathbf{E}}{\partial t} &= \nabla \times \mathbf{B} - \mathbf{J}. \end{aligned} \tag{2.4}$$

Substituting the expansions for each field into these equations, the following equations for each mode m satisfies

$$\begin{aligned} \frac{\partial B_r^m}{\partial t} &= -\frac{im}{r} E_z^m + \frac{\partial E_\theta^m}{\partial z}, \\ \frac{\partial B_\theta^m}{\partial t} &= -\frac{\partial E_r^m}{\partial z} + \frac{\partial E_z^m}{\partial r}, \\ \frac{\partial B_z^m}{\partial t} &= -\frac{1}{r}\frac{\partial}{\partial r}(r E_\theta^m) + \frac{im}{r} E_r^m, \\ \frac{\partial E_r^m}{\partial t} &= \frac{im}{r} B_z^m - \frac{\partial B_\theta^m}{\partial z} - J_r^m, \\ \frac{\partial E_\theta^m}{\partial t} &= \frac{\partial B_r^m}{\partial z} - \frac{\partial B_z^m}{\partial r} - J_\theta^m, \\ \frac{\partial E_z^m}{\partial t} &= \frac{1}{r}\frac{\partial}{\partial r}(r B_\theta^m) - \frac{im}{r} B_r^m - J_z^m, \end{aligned} \tag{2.5}$$

where all quantities are complex functions of (r, z).

We can see that the Eqs. 2.5 are linear, so that the only coupling between the modes has to come through the source term J. In particular each mode propagates independently in vacuum, and in a linear medium. However, modes coupling appears either if the medium is non-uniform in the transverse plane (not considered here) or from non-linearities in the current.

In PIC calculations, the current is given by the sum of the contributions of macro-particles. These particles obey the relativistic equation of motion

$$\begin{aligned} \frac{d\mathbf{P}}{dt} &= -q(\mathbf{E} + \mathbf{v}/c \times \mathbf{B}), \\ \frac{d\mathbf{x}}{dt} &= (1/m\gamma)\mathbf{P}, \end{aligned} \tag{2.6}$$

where q and m being macro-particle charge and mass. From Eq. 2.6, we see that non-linearities appear from non-local effects, the laser intensities being non uniform, and from relativistic effect through the term $\mathbf{v} \times \mathbf{B}$. The important point is that these non-linearities depend on the fields modules, which are independent of the polarization direction and remain mainly axisymmetric. So that, even with a significant level of non-linearity, the symmetry of the physical system is conserved. This is no longer the case in high density targets and at ultra-high laser intensities. Here we only consider targets with densities much lower than the critical one and laser intensities lower than $10^{19}\mathrm{W.cm}^{-2}$. In such cases, keeping only the $m = 0, 1$ modes is well justified. Technically in WARP, the numerical implementation of the algorithm used to solve Eqs. 2.5 and 2.6 follows the description given in [4].

3. Electron beam characteristic in relation with experimental results

WARP with the Fourier decomposition algorithm was used to simulate the experiment described in [3]. In this experiment, the target is a mixture of gases ($H_2 + N_2$), therefore a field ionization module based on ADK model [5] was introduced in WARP to model ionization dynamics. A summary of the parameters used in our calculations is given in Table 1.

Table 1: List of parameters

Plasma density on axis	n_{e0}	$7.8 \times 10^{18}\,\mathrm{cm}^{-3}$
Plasma length	L_p	2.5 mm
Gas composition		99%H + 1%N
Laser profile		Gaussian
Normalized vector potential	$a_0(z_f)$	1.1
Laser wavelength	λ	0.8 μm
Laser spot size (FWHM)	σ	17 μm
Laser duration (FWHM)	τ	40 fs
Laser focal position	z_f	0.9 mm
Laser polarization		*linear*
Number of Fourier modes		2
Number of particles/cell		36 macro
Cell size in r	δr	$1.25\lambda/2\pi$
Cell size in z	δz	$0.05\lambda/2\pi$

In this table $a_0(z_f)$ is the maximum value of the laser amplitude in normalized units: $a_0(z) = \max_{r,t}\left[\frac{ea(r,z,t)}{m_e\omega c}\right]$, where ω is the laser frequency, e the electron charge and m_e the electron mass. The value of 1.1 corresponds to the focal plane $z = z_f$, without plasma.

As will be seen below, the density profile has a strong influence on the electron trapping and acceleration processes. In our simulation, we used directly the experimentally determined profile as given in [3].

3.1. Electron beam energy spectrum

We first compare, in Fig. 1, the experimental electron beam energy spectrum with the simulated one, determined at the exit of the target.

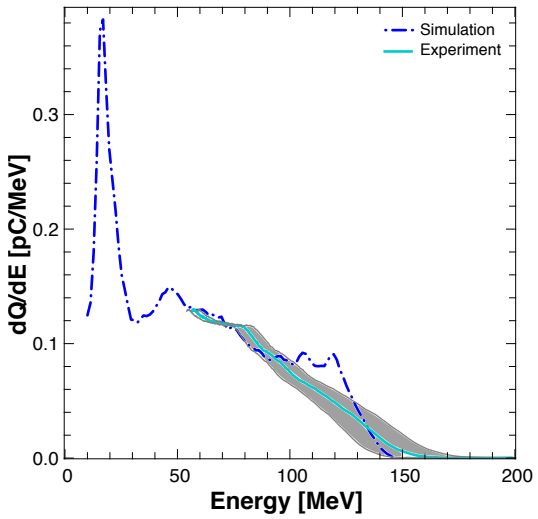

Figure 1: Comparison between simulated and experimental electron beam energy spectrum. The simulated energy spectrum is normalized by the experimental energy spectrum value at 50MeV. The experimental result has an energy cutoff at 50MeV. The grey area represents experimental errors.

We observe in this figure that the electron beam has a rather large energy distribution suggesting a continous injection of electrons, with the highest energy extending to ≈ 150MeV. The simulated spectrum has a maximum energy within the experimental error bars, it also reproduces well, above 50MeV, the experimental shape of the curve. This shows a good agreement between the experiment and the simulation results. Moreover, the simulation exhibits a peak at 17MeV with an FWHM energy spread, $\Delta E/E \approx 69\%$.

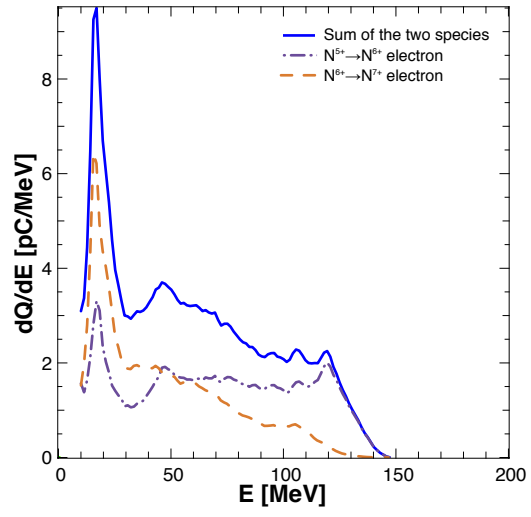

Figure 2: Contribution of different electron species in the final electron beam energy spectrum.

In Fig. 2, is reported the contribution of the different species of electrons in the total spectrum. We observe that only the two electrons, initially in the K shell of nitrogen, are accelerated to high energies. The other electrons coming either from nitrogen or from hydrogen are not trapped but contribute in building the plasma wake. This is in agreement with the 3D OSIRIS particle-in-cell code results [6]. Note also that electrons coming from the helium like ion yield the main contribution to the highest part of the spectrum, while those from the hydrogenic ion contribute mainly to the low energy peak.

3.2. Emittance

The divergence and emittance are two important characteristics of the emitted electron beam. We have reported in Fig. 3, the phase space in $x-$ and $y-$directions of the electron bunch at the exit of the target, the electron momentum being normalized by $m_e c$. From these data we have deduced a full width at half maximum (FWHM) divergence of $\approx$ 1mrad in x-direction and 4.6mrad in y-direction, whereas the emittance [7], are respectively of $\epsilon_x = 1.4$mm.mrad and $\epsilon_y = 30.4$mm.mrad. The higher values in the $y-$direction are related to the polarization of the laser field. In fact after tunnel ionization the electron acquires a quiver velocity in the direction of the polarization.

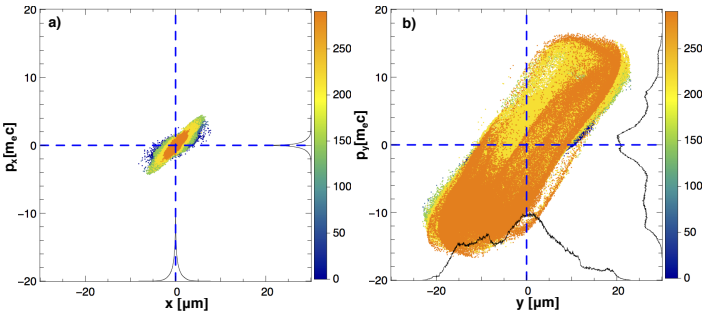

Figure 3: A set of points representative of an electron beam in the a) $(x, p_x)-$, b) $(y, p_y)-$phase space. The color bar represents the relative density of the electrons.

3.3. Beam dynamics

In order to analyze the previous results, we have looked at the correlation between the injection process and the acceleration one.

In Fig. 4, we have plotted the final energy of the electrons as a function of their trapping position. We see a significant correlation between these two quantities. As the trapping position increases, the distance of acceleration decreases and in fact only electrons trapped at the early stage can be accelerated to the highest energy. In particular the electrons coming from the hydrogenic ion have lower energies, in accordance with Fig. 2, because they are trapped later. We observe also in Fig. 4 that the position-energy correlation is not perfect. In particular, for the high energy part, we can observe that electrons having a difference of more than 100μm in the trapping positions, can finally get the same final energy.

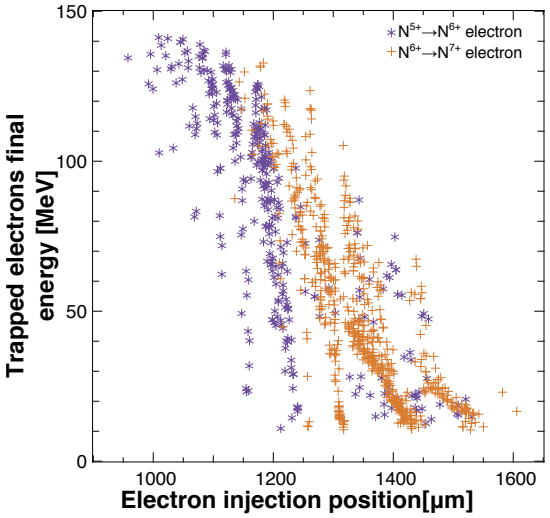

Figure 4: Trapped electrons final energy are plotted against their injection position. Electrons are chosen with an energy, $E \geq 10$MeV at the exit of the target.

3.4. Laser amplitude and plasma wave

In order to explain the data of Figs. 2 and 4, we now look at the evolution of the laser amplitude and of the plasma wave, which are responsible both for the trapping and for the acceleration process. In Fig. 5(a), we have plotted the evolution of $a_0(z)$ during propagation together with the density profile of the target. The focal plane of the laser z_f is at 900μm, at the entrance of the target, where the density is rapidly increasing. Relativistic self-focusing dominates over diffraction when $\alpha = P_L/P_C \gtrsim 1$, P_L being the maximum value of the laser power and $P_C(z)$ the value at z, of the critical power for relativistic self-focusing [8]. Close to the target entrance, P_L remains nearly constant while $P_C(z)$, being inversely proportional to the density, strongly decreases with z. Therefore α increases rapidly and becomes higher than 1. The value of α however does not become very large, therefore the self-focusing is rather smooth, the maximum of intensity being reached close to the target exit. In Fig. 5(a) vertical lines mark 3 positions, corresponding to (1) the start of the trapping process, (2) the maximum value of $a_0(z)$ and (3) the end of the trapping process. We can observe that the domain of trapping corresponds also to the domain of high target density. Therefore, in our conditions, the density profile appears as the dominant parameter controlling the trapping process.

In Figs. (5(b) are reported the laser fields and the plasma wave amplitudes on axis at the three positions. We can see that at position (1) we are in a quasi-linear regime, where the laser pulse is still Gaussian and the plasma wave periodic. At the maximum of the laser intensity, position (2), non-linearities become apparent, both on the plasma wave and also on the deformation of the laser pulse. The accelerating field has been increased, taking into account the additional normalization factor which depends on the

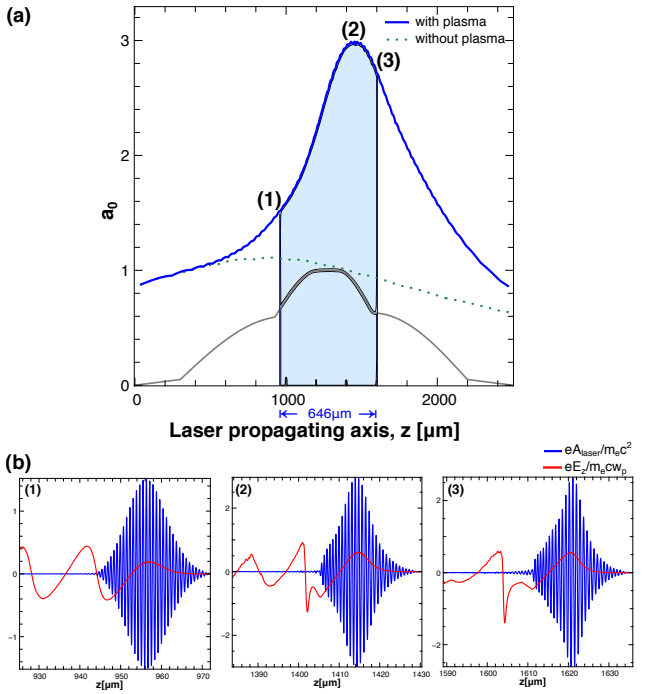

Figure 5: (a) The evolution of a_0, we define three phases: (1) the beginning of injection, (2) the a_0 is maximum, (3) the end of injection. The shaded region represents the injection range. The grey line shows the longitudinal density profile of the gas cell. (b) The vector potential of the laser, A_{laser} normalized to $m_e c^2/e$ and the wakefield, E_z normalized to $m_e c w_p/e$ at phases (1), (2) and (3).

density, and a peak at the back of the first oscillation behind the laser is visible. This peak is due to the field generated by the trapped electrons. Beam loading effects are therefore significant in our case. Position (3) is similar to the second one. However, due to the decrease in density, and also in $a_0(z)$, the amplitude of the electrostatic field has been decreased, while the relative contribution of the beam loading effect has increased, due to the accumulation of trapped charges.

Information on the transverse properties of the laser and plasma wave structure at the three positions is given in Fig. 6.

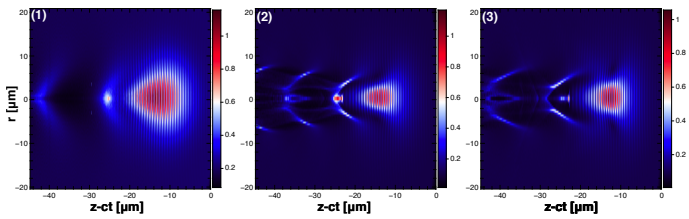

Figure 6: Electronic density map together with the laser amplitude at the three positions reported in Figure 5.

Fig. 6(1) confirms the fact that at the beginning of the injection, we are in a quasi-linear regime, in particular the transverse size of the plasma wave is similar to the laser pulse one. At this position, the laser ponderomotive force

is not strong enough to expel all plasma electrons from the vicinity of the axis. On the contrary, at position (2), the transverse size of the laser pulse is minimum leading to the highest field amplitude $a_0 \approx 3$. A full matched blown-out structure can then be formed, yielding the highest accelerating field. At position (3) the transverse size of the laser pulse has increased again, diffraction becoming dominant over self-focusing, leading to a decrease of the laser intensity.

Concerning the trapping of electrons coming from N^{6+}, the simulation shows that, due to their strong binding energy, these ions are ionized only for the highest values of $a_0(z)$. The principal trapping condition for these electrons become simply that they have to be generated, but once created they are even more easily trapped than the electrons coming from N^{5+}.

From the presented results, the fact that electrons with quite different trapping position get the same final energy can be explained by the following: first a strong increase of the accelerating field, occurring after the trapping, meaning that the main part of the energy is gained at the end of the acceleration process, so that the final energy is less sensitive to the initial part of this acceleration; second, the first trapped electrons when accelerated, will move toward the front of the bubble, whereas newly generated electrons will be trapped at the back of the bubble where the accelerating field reached a higher value.

4. Conclusion

We have presented the modeling of a laser-driven plasma acceleration experiment with WARP using the Fourier decomposition algorithm.

Using a realistic density profile has allowed to perform direct comparisons with experimental results, which show good agreement. This is also the case for the other experimental data, using the same set-up and presented in [3]. Therefore the validity of the code is confirmed, and in particular the fact that, in the considered conditions, accurate results can be obtained with only two Fourier harmonics. The detailed analysis of the simulation results has allowed to get more insights of the electron trapping and acceleration process when the ionization-induced injection and density gradient effects are combined. The high efficiency of the quasi-3D model has allowed to perform a direct parametric investigation for optimizing the electron beam properties, which results will be published in a forthcoming paper.

5. Acknowledgments

We acknowledge the use of the computing facility cluster GMPCS of the LUMAT federation (FR LUMAT 2764) and the partial financial support of the Laboratoire d'Excellence PALM, within the `Model_LPA` project.

6. References

[1] J-L Vay, D P Grote, R H Cohen, and A Friedman. Novel methods in the particle-in-cell accelerator code-framework warp. *Computational Science & Discovery*, 5(1):014019, 2012.

[2] A.F. Lifschitz, X. Davoine, E. Lefebvre, J. Faure, C. Rechatin, and V. Malka. Particle-in-cell modelling of laserplasma interaction using fourier decomposition. *Journal of Computational Physics*, 228(5):1803 – 1814, 2009.

[3] T. L. Audet et al. Investigation of ionization-induced electron injection in a wakefield driven by laser inside a gas cell. *submitted*, 2015.

[4] A. Davidson, A. Tableman, W. An, F.S. Tsung, W. Lu, J. Vieira, R.A. Fonseca, L.O. Silva, and W.B. Mori. Implementation of a hybrid particle code with a {PIC} description in rz and a gridless description in into {OSIRIS}. *Journal of Computational Physics*, 281:1063 – 1077, 2015.

[5] M.V Ammosov, N.B Delone, and V. Krainov. Tunnel ionization of complex atoms and of atomic ions in an alternating electric field. *Sov. Phys. JETP*, 64:1191, 1986.

[6] A. Pak, K. A. Marsh, S. F. Martins, W. Lu, W. B. Mori, and C. Joshi. Injection and trapping of tunnel-ionized electrons into laser-produced wakes. *Phys. Rev. Lett.*, 104:025003, Jan 2010.

[7] J. Buon. Beam phase space and emittance. *LAL-RF-90-15-REV, LAL-RT-92-03, CAS-CERN Accelerator School: 5th General Accelerator Physics Course, pp.89-116*, Feb, 1992.

[8] Gerard A. Mourou, Toshiki Tajima, and Sergei V. Bulanov. Optics in the relativistic regime. *Rev. Mod. Phys.*, 78:309–371, Apr 2006.